communications earth & environment

ARTICLE

https://doi.org/10.1038/s43247-023-01149-x OPEN

Gas buffering of magma chamber contraction during persistent explosive activity at Mt. Etna volcano

Daniele Carbone [1✉], Flavio Cannavò [1], Chiara Paola Montagna [2] & Filippo Greco[1]

A sequence of more than 20 short-lasting explosive eruptions took place at Mt. Etna volcano, during a 2-month period in 2021. Here we perform a joint analysis of the gravity decrease and ground deflation that accompanied the sequence of eruptions. Results from this joint analysis are cross-checked against the output of a numerical code providing independent geochemical insight on how the density of the magmatic liquid/gas mixture in the source reservoir varies as a function of the pressure. This cross-analysis provides a framework to explain why (i) the bulk volume reduction sensed by the ground deformation data is much lower than the volume of the erupted products and (ii) the observed gravity changes point to a strong mass decrease, incompatible with a pure mechanism of magma withdrawal. We conclude that pressure-driven gas exsolution and expansion compensated the withdrawal of magma, thus buffering the contraction of the source reservoir and leading to the inferred mass decrease.

[1] Istituto Nazionale di Geofisica e Vulcanologia, Sezione di Catania - Osservatorio Etneo, Catania, Italy. [2] Istituto Nazionale di Geofisica e Vulcanologia, Sezione di Pisa, Pisa, Italy. ✉email: daniele.carbone@ingv.it

2021 was an exceptional year of eruptive activity at Mt. Etna, with nearly 60 paroxysmal explosive episodes (lava fountains[1]) occurring from one of the volcano's summit craters (SEC; see inset in Fig. 1).

Here, we perform a joint analysis of continuously recorded gravity and ground deformation data, aimed at shedding new light on the bulk processes that took place during the occurrence of a series of lava fountains events closely spaced in time. The gravity data we utilize were acquired through three continuously recording gravimeters, installed at different sites. In particular, time series from iGrav#16 and iGrav#20 superconducting gravimeters (SGs), installed at SLN and MNT stations[2] (Fig. 1), respectively, were employed. Furthermore, we consider the gravity time series from AQG-B03 absolute quantum gravimeter, installed at PDN station[3] (Fig. 1). Gravity data are corrected for environmental effects (Earth tide, polar motion, atmospheric pressure, ground tilt) and, in the case of AQG-B03, possible instrumental drifts (drift of the radio frequency reference and drift of the laser frequency[3]).

Ground deformation data come from the continuously operating GNSS network of Mt. Etna, which includes permanent stations across the whole volcano edifice[4] (Fig. 1). Raw GNSS data are recorded through Leica Geosystems instruments and processed on a daily basis, using the GAMIT/GLOBK software[5]. The processed GNSS solutions are referred to the geodetic reference frame, specifically designed for the Etnean area[4,6].

In order to ease the joint analysis of gravity and GNSS data and reduce the higher-frequency noise, daily averages of all the available data were calculated. Figure 2 shows 160-day of gravity and deformation (vertical component) time series, between 16 May and 23 October 2021. One of the most striking common features is the phase of gravity decrease and deflation which occurred during early June to late July (marked with the yellow band in Fig. 2). Figure 2 also reports the timing of the 38 lava fountain events that occurred during the considered period (orange marks in the upper part of the figure). Among these, more than 20 episodes occurred during early June to late July[1].

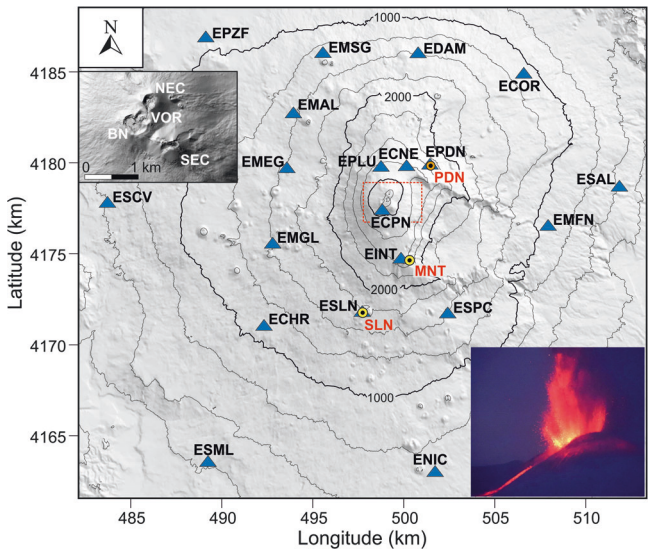

Fig. 1 Map of Mt. Etna showing the position of the gravity and GNSS stations for continuous data acquisition. Blue triangles: GNSS stations; circles: gravity stations. Different colors are used for PDN (orange) and for SLN and MNT (yellow) to highlight the different types of gravimeters utilized: SGs at SLN and MNT, an AQG-B at PDN. Note that, while SLN and PDN gravity stations are colocated with GNSS stations, MNT is ~500 m away from the closest GNSS station (EINT). The inset at the top left shows a detail of the area inside the dotted rectangle, including the summit active craters of Mt. Etna (NEC Northeastern Crater, VOR Voragine, BN Bocca Nuova, SEC Southeastern Crater, redrawn from Sciotto et al.[19]). The inset at the bottom right is a photo taken during one of the lava fountains in June 2021.

The horizontal and vertical components of the deformation field during 07 June to 31 July 2021 are shown in Fig. 3a, b, together with the amplitude of the gravity changes observed at the three stations during the same period (Fig. 3c). The start and end dates of this period (yellow band in Fig. 2) were chosen with a view to (i) obtaining a deformation field as coherent as possible, (ii) including most of the phase when the gravity signals decrease at a higher rate, (iii) including the cluster of lava fountains that occurred at intervals of <1 to a few days, throughout June and July (Fig. 2). Only the 20 GNSS stations closest to the summit craters are considered (Fig. 1), since variations that are either negligible or unrelated to volcanic processes were observed at the other sites. Overall, the GNSS data depict an almost radial pattern toward the summit craters area (Fig. 3a). We consider an uncertainty of 1 and 3 cm, associated with the horizontal and vertical components of GNSS data, respectively[7]. The amplitude of the observed 07 June–31 July 2021 gravity decrease is progressively higher as one approaches the summit craters (Fig. 3c). The uncertainties on the time gravity changes observed at the 3 stations (error bars in Fig. 3c) are propagated from uncertainties affecting the daily gravity averages on 07 June and 31 July. In turn, the latter uncertainties are defined as the standard deviation of the daily averages within a 15-day window centered at the selected date.

The calculated uncertainties on the time gravity changes are about 1, 4, and 8 μGal, at SLN, MNT, and PDN, respectively, and include possible effects due to instrumental drift on the SGs at SLN and MNT stations. In particular, the instrumental drift on iGrav SGs is expected[8] to be <5 μGal/year, implying an effect of about 0.7 μGal over the considered 55-day period.

Results

Data inversion results. The net gravity changes and deformation over the period indicated with the yellow band in Fig. 2 are jointly inverted using a convergent Pattern Search Algorithm[7,9,10]. The latter iteratively generates an adaptive grid of model parameters and searches for the parameters which provide the best fit between observed and synthetic data. The best parameters are estimated by minimizing the objective function (see "Methods"), defined as a weighted mean of squared residuals[7]. In turn, the residuals are weighted by the inverse of the uncertainty associated with the measurements. The radial pattern of the early-June–late-July deformation field (Fig. 3a) led us to choose the analytical expressions of Mogi[11] as forward model of the bulk mass and pressure changes, as already done in previous studies[12,13]. The effect of topography on the observed deformation is accounted for using the varying-depth model[14]. As for gravity data, they are inverted for the total mass change taking place in the source volume (ΔM), rather than for the density of the fluid involved in the source process. Under the far-field approximation, we consider the following form of the Mogi[11] formulation:

$$\begin{aligned} u_r &= \Delta V \frac{(1-\upsilon)}{\pi} \frac{r}{R^3} \\ u_z &= \Delta V \frac{(1-\upsilon)}{\pi} \frac{d}{R^3} \\ \Delta g &= G\Delta M \frac{d}{R^3} + \gamma \Delta h \end{aligned} \quad (1)$$

where, u_r and u_z are horizontal and vertical deformation, Δg is

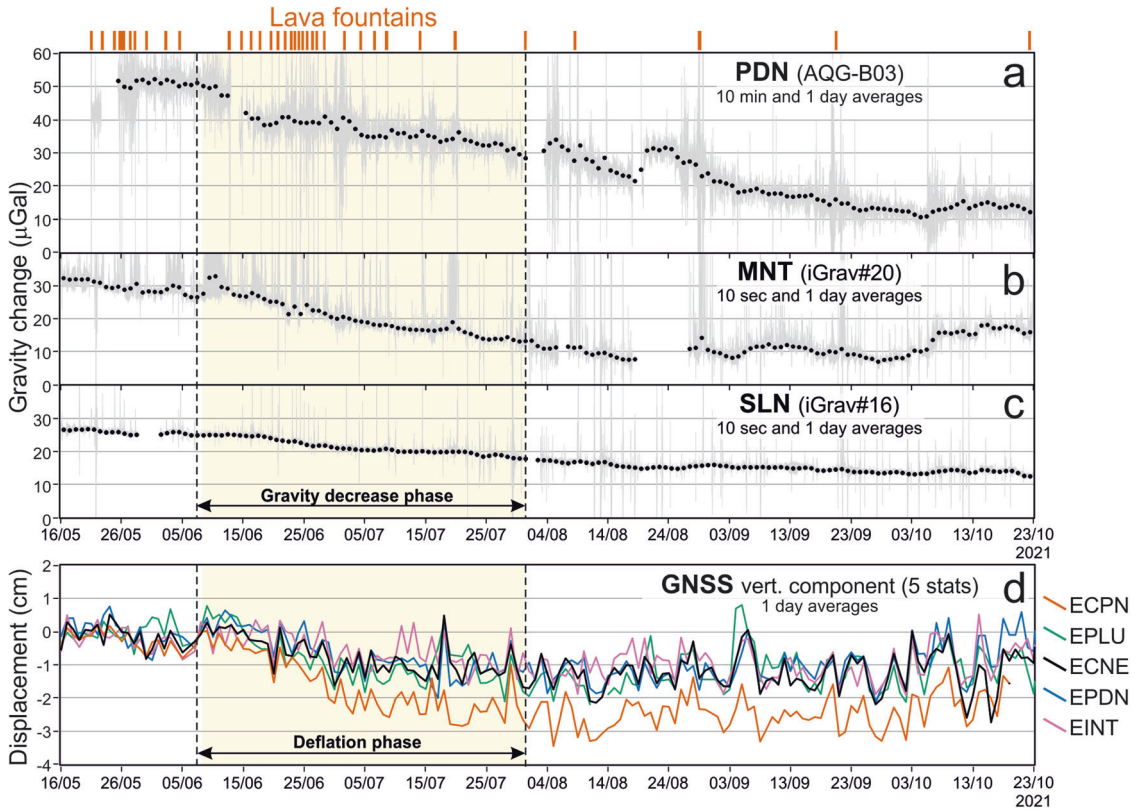

Fig. 2 Gravity and vertical deformation time series. Upper block: gravity time series from PDN **a**, MNT **b**, and SLN **c**, during 16/05 to 22/10/2021. All gravity data were corrected for the effect of known perturbations (see text for details) and are supposed to reflect only underground mass changes. At PDN, gravity data were acquired through AQG-B03; 10 min and 1day averages are shown in **a**. At MNT and SLN, gravity data were acquired through iGrav#20 and iGrav#16 SGs, respectively; 10 s and 1-day averages are shown in **b**, **c**. Lower block (**d**): GNSS time series (vertical component) from the 5 stations closest to the summit craters (see Fig. 1). The orange marks in the uppermost part of the figure indicate the timing of the lava fountains that occurred during the considered period.

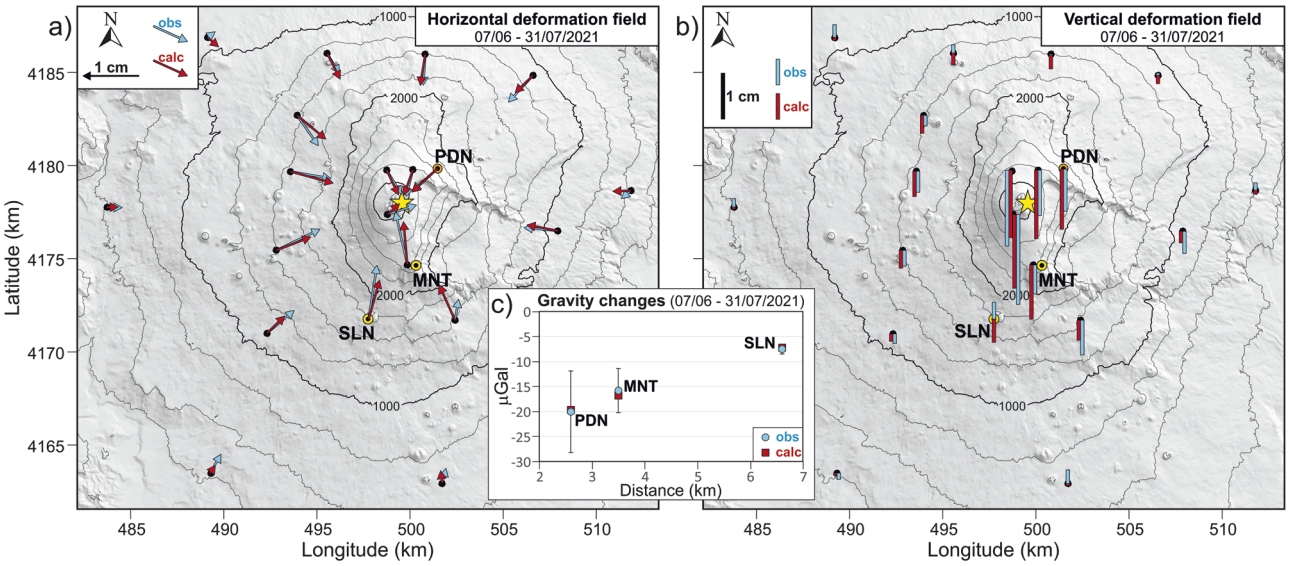

Fig. 3 Observed and calculated deformation field and time gravity changes. a Horizontal component of the observed (blue vectors) and calculated (red vectors) deformation field, during 7 June to 31 July 2021. The yellow star marks the position of the modeled source (Table 1). **b** Same as **a**, but for the vertical component of the deformation field. **c** Observed (light blue dots) and calculated (red squares) gravity changes at SLN, MNT, and PDN, during the same period as **a**, **b**, plotted against the horizontal distance between each station and the vertical projection of the modeled source. The error bars represent uncertainties on the time gravity changes (see text for details on how the uncertainties are calculated).

Table 1 Results of the joint inversion.

Parameter (unit)	East (km)	North (km)	Depth (km b.s.l.)	ΔV (10^6 m^3)	ΔM (10^{11} kg)
Lower bound	450	4150	−10	−10	−5
Upper bound	520	4190	0	10	5
Best fit	499.61 ± 0.14	4177.94 ± 0.18	−2.64 ± 0.18	−2.27 ± 0.32	−1.42 ± 0.15

Optimal solution parameters and boundaries of the search ranges. In the bottom row (best fit parameters), the 2-σ uncertainties, calculated by jackknifing[42], are also reported.

the gravity change observed at the surface, ΔV is the source volume change, v is the Poisson's ratio, G is the universal gravity constant, d is the depth to the center of the source, R is the distance between the center of the source and the surface observation point, γ is the free air gradient (standard value = −0.3086 mGal/m) and Δh is the observed vertical deformation. All model parameters are simultaneously retrieved by the inversion procedure. It is important to stress that gravity data are not corrected for elevation changes before they are fed to the inversion scheme. Instead, these corrections are performed at each iteration of the inversion process, using modeled, rather than observed, vertical deformation. This relaxes the stringent need of elevation control at each gravity station, which arises when the classical procedure is employed, and allows the exploitation of gravity data from stations that are not colocated with GNSS stations, as in the case of MNT (see Fig. 1).

Inversion results are shown in Table 1 and Fig. 3. The modeled source is placed beneath the summit craters of Mt. Etna (Fig. 3), at a depth of about 2.6 km b.s.l. The observed ground deformation is driven by a bulk volume reduction of about 2.3×10^6 m^3, while the observed gravity changes reflect a bulk mass decrease of about 1.4×10^{11} kg (Table 1).

Interpretation of the inversion results. Results of the joint modeling (Table 1) indicate that the volume change inferred from the deformation is only ~5% of a conservative estimate ($\Delta M/\rho$) of the volume change inferred from the observed gravity variations (if ρ is assumed[15] to be equal to 2800 kg/m^3, $\Delta V \approx 50 \times 10^6$ m^3). This indicates the activation of a mechanism allowing mass loss to occur without the expected corresponding deformation. Likely, the observed gravity changes were driven by a density change of the magma already present in the reservoir that underwent the volume reduction. Excessive mass gain/loss was observed at several volcanoes[16] and different processes were proposed to explain it, including[17] compression or decompression of the magma in the reservoir, substitution of the resident magma with magma of different density, filling/emptying of void space. In the present case, a further constraint on the mechanism behind the observed changes comes from the estimated volume of erupted products during the study period. An average DRE volume of erupted tephra of 0.9×10^6 m^3 was reported[1] for each lava fountain. The DRE volume was calculated as 0.18% of the total volume of erupted gas and pyroclastics[18]. In turn, the total volume is retrieved as the product of (i) the duration of the lava fountain, (ii) the mean fluid exit velocity at the vent (a linear function of the fountain height), and (iii) the vent surface area. While the duration and average height of each fountain was obtained by analyzing the images from the thermal and visual cameras installed on the volcano slopes[1], the vent area was calculated assuming a circular shape and a diameter of 30 m[18]. This size is not entirely in keeping with more recent structure-from-motion mapping results[19]. Since the erupted volume scales with the square of the vent size, even small differences in the assumed vent radius may lead to important changes in the estimated tephra volume. These considerations imply that the volume of erupted tephra should be treated as indicative, rather than a precise estimate, also considering the uncertainty on the above 0.18% factor.

To obtain a complete estimate of the erupted products, the volume of the lava flows that occurred during the fountaining events must also be accounted for. Using in-situ, drone, and satellite observations, an average of 0.8×10^6 m^3 was obtained for the volume of each lava flow during the study period[20]. Hence, for the 22 eruptions during early-June to late-July, it results a total erupted volume of slightly less than 40×10^6 m^3. This value is more than an order of magnitude larger than the source volume reduction resulting from the joint inversion (Table 1), while it is comparable to the volume change inferred from the observed gravity variations, within the above uncertainties. This observation leads us to favor a mechanism behind the gravity changes somehow related to the extraction, from the reservoir, of the magma that fed the eruptions. We thus rule out that the replacement of denser resident magma, sinking to deeper levels, by rising magma with a lower density[21] may be the primary cause of the recorded gravity decrease. It also seems unrealistic that the erupted material may have left void space under the confining pressure at depths of 5–6 km beneath the surface.

Conversely, a viable possibility is that the observed gravity decrease was driven by a decompression-related density change, i.e., an increase in the proportion of exsolved gas to magma in the source reservoir, resulting in an overall increase of bulk magma compressibility. Indeed, it is likely that the pressure decrease, consequent to progressive magma extraction from the reservoir during the eruptions, caused gas exsolution and expansion of both the pre-existing and the newly-exsolved gas phase. In turn, the new gas buffered the reservoir contraction, thus leading to the relatively small volume change measured through GNSS.

A constraint on the early-June to late-July pressure decrease can be retrieved from the inversion results shown in Table 1, through the following expression[22,23]:

$$\Delta P \cong \frac{\mu \Delta V}{\pi a^3} \tag{2}$$

where, ΔP is the pressure change, μ is the shear modulus, ΔV the volume change derived from the joint inversion (Table 1) and a is the radius of the source reservoir, assumed to be spherical shaped. It also holds that[24]:

$$\Delta M = \left(\rho' - \rho_r\right)\Delta V + \Delta\rho V \tag{3}$$

where, ΔM is the mass change derived from the joint inversion (Table 1), $\rho' - \rho_r$ is the density difference between magma lost from the reservoir and host rock, $\Delta\rho$ is the density change within the source and V is the volume of the source reservoir. It is worth stressing that ρ' represents the original magma density, before $\Delta\rho$ occurs. Even if a relatively large value is assumed for $\rho' - \rho_r$ (e.g., 500–1000 kg/m^3), the absolute value of the first term to the right of the equal sign remains on the order of $1–2 \times 10^9$ kg, thus, about two orders of magnitude smaller than the absolute value of ΔM resulting from the joint inversion (1.4×10^{11} kg; Table 1). Hence,

this term can be neglected in Eq. 3:

$$\Delta M \cong V\Delta\rho \cong \frac{4}{3}\pi a^3\Delta\rho; \pi a^3 \cong \frac{3\Delta M}{4\Delta\rho} \quad (4)$$

Substituting Eq. 4 in Eq. 2, we can express the density change within the source volume as a function of the pressure change:

$$\Delta\rho \cong \frac{3\Delta M}{4\mu\Delta V}\Delta P \quad (5)$$

The dashed black line in Fig. 4 shows the $\Delta\rho/\Delta P$ relation (Eq. 5), for the values of ΔM and ΔV constrained by the joint inversion of deformation and gravity data (Table 1) and for a value of μ of 30 GPa (the value most commonly used in modeling works focused on Mt. Etna[25]).

An independent estimate of the relationship between $\Delta\rho$ and ΔP is obtained using the SOLWCAD code[26], which computes volatile saturation as a function of pressure, temperature, and silicate melt composition, under the assumption of thermodynamic equilibrium between the liquid and exsolved phases. Computations with SOLWCAD are performed assuming a constant temperature of 1373 K[27], and initial pressure within the reservoir of 140 MPa, roughly corresponding to a depth of 3 km b. s. l. (Table 1). Compositional data in Table 2, measured from a melt inclusion in products of the 2001 eruption[28], represent a typical composition for Etnean magmas and are input to the thermodynamical model. Slight variations in oxide composition from different samples[28], or in magma temperature, do not affect significantly volatile saturation[26] and density of the multiphase magma.

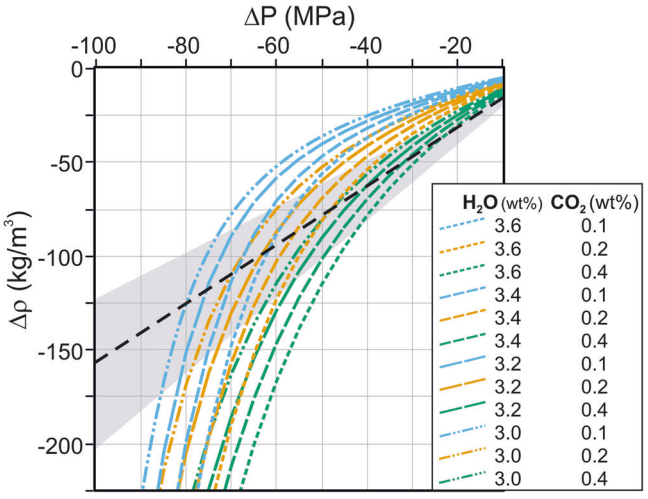

Fig. 4 Comparison between geophysical inversion results and geochemical modeling data. Dashed black line: $\Delta\rho/\Delta P$ relation of Eq. 4, for the values of ΔM and ΔV reported in Table 1 and for a value of μ of 30 GPa[25]. The gray area gives the uncertainty on the $\Delta\rho/\Delta P$ relation, propagated from uncertainties on ΔM and ΔV (Table 1). Colored dashed lines: estimates of the $\Delta\rho/\Delta P$ relation obtained using the SOLWCAD code[26]. The main oxide contents reported in Table 2 and the H_2O and CO_2 contents reported in the figure are used as inputs to the SOLWCAD code.

Initial contents of H_2O and CO_2 of 3 to 3.6 wt% and 0.1 to 0.4 wt%, respectively, are assumed in the calculation[27–29]. Measured volatile contents have been obtained from melt inclusions, implying that they represent a lower limit for total contents in the magma, as they only include dissolved amounts. Indeed, since Etnean magmas are typically gas-rich[29], exsolved volatiles are expected to be present at the relatively shallow depth of the inferred reservoir (Table 1).

The density of the two-phase mixture (ρ_{mix}) at each pressure step is evaluated as:

$$\frac{1}{\rho_{mix}} = \frac{n}{\rho_g} + \frac{1-n}{\rho_l} \quad (6)$$

where, n is the weight fraction of exsolved gas in the mixture, while ρ_g and ρ_l are pressure-dependent densities of the gas and liquid phases, respectively, calculated through suitable models[30,31]. Results from SOLWCAD are also presented in Fig. 4 (colored lines). Overall, changes in ρ_{mix} are dominated by gas exsolution and expansion, with respect to the relatively small (up to 5%) contribution due to variations in ρ_l. Indeed, SOLWCAD predicts that, under the assumed conditions (Table 2 and Fig. 4), the volume fraction of gas increases from almost zero to about 30%.

From Fig. 4, it appears that the $\Delta\rho/\Delta P$ curve, obtained from the results of the geophysical data inversion (dashed black line), crosses the curves predicted by the geochemical model at values of ΔP ranging between about 25 (for the highest assumed initial contents of H_2O and CO_2) and 80 MPa (for the lowest assumed initial contents of H_2O and CO_2). Hence, under the assumptions described above, a pressure decrease within this range of values should develop to induce the increase in the amount of exsolved gas which (i) buffered the contraction of the reservoir, thus leading to the strong difference between magma chamber volume reduction and erupted volume and (ii) played a major role in causing the observed gravity (hence, mass) change.

Large amounts of CO_2 fluxing[28] from deeper levels to the inferred reservoir at ~2.6 km b.s.l. would likely lead to different results, by changing the characteristics of the geochemically-derived $\Delta\rho/\Delta P$ curves. However, we neglect this effect due to the lack of quantitative data on gas fluxing at Mt. Etna, over time scales of the order of a few months.

It is important to note that the inferred depressurization can induce mechanical instability of the reservoir walls. Some authors[32] proposed that failure initiates when the difference between reservoir pressure and lithostatic pressure at reservoir depth reaches the strength of rocks. For volcanic rocks, the tensile strength does not usually exceed 20 MPa[33], implying that the scenario suggested by our results (pressure in the source volume decreasing by ≥ 25 MPa) would not be viable from the point of view of the mechanical stability of the reservoir. However, geometrical considerations (i.e., chamber size and depth) must be taken into account when evaluating the mechanical stability of a depressurizing magma chamber. The two edge values of the inferred range of pressure decreases (25 and 80 MPa; Fig. 4) correspond to source radii of 950 and 645 m, respectively (Eq. 2), and, considering the estimated source depth of about 5.6 km under the surface, to a radius-to-depth ratio between 0.1 and 0.2.

Table 2 Main oxides contents (wt. %) in the silicate melt.

SiO_2	TiO_2	Al_2O_3	Fe_2O_3	FeO	MnO	MgO	CaO	Na_2O	K_2O
43.88	1.88	16.49	2.12	7.96	0.18	5.58	10.77	3.27	2.07

Main oxides contents[28] used for the calculation of the multiphase magma density and volatile partitioning. Reported data are from melt inclusion analyses. The partitioning between FeO and Fe_2O_3 has been calculated assuming[41] $Fe_2O_3/FeO = 0.2$.

Table 3 Results of the joint inversion with the ECM.

Param. (unit)	East (km)	North (km)	Depth (km)	ω_x (°)	ω_y (°)	ω_z (°)	a_x (km)	a_y (km)	ΔV (10^6 m^3)	ΔM (10^{11} kg)
Lower bound	450	4150	−10	0	0	0	0	0	−10	−5
Upper Bound	520	4190	0	360	360	360	2	2	10	5
Best fit	499.62	4178.07	−2.80	0	32	144	0.82	1.40	−2.32	−1.49

Optimal solution parameters from the joint inversion of the ground deformation and gravity data, using the ECM[39] as the forward model. ω_x, ω_y and ω_z are the rotation angles of the ellipsoidal cavity, while a_x and a_y are its semi-axes (the third semi-axis, a_z, was fixed equal to 1 km in the calculations).

For such underpressure and geometrical conditions, neither tensile[34], nor shear[33,35] failure of the reservoir walls are expected to occur.

Conclusions

Previous joint inversions of gravity and ground deformation data were based on discrete gravity measurements, implying that only variations occurring over time scales on the order of several months to years could be taken into account[13,16,36]. The availability of high quality time-series from driftless (the AQG-B[3]) and almost driftless (the iGrav SG[8]) continuously recording gravimeters offers the possibility to precisely detect even small gravity changes associated with ground deformation, occurring over a wide range of time scales. Indeed, the gravity changes in the focus of the present study developed over a period of less than 2 months (Fig. 2) and have amplitudes that range between about 7 and 20 μGal (Fig. 3). Importantly, such changes would be hardly detected, if at all, through continuous measurements from the more widely utilized spring gravimeters, due to the overwhelming effect of the instrumental drift on the signal from these devices[37].

The joint inversion of the changes observed during early June to late July 2021 provides a framework to better understand the volcanic processes that occurred during a period when more than 20 lava fountains took place (Fig. 1). Each fountaining episode erupted a volume of between 1 and 2×10^6 m^3 of pyroclastics and lava[1,20], implying that the total erupted volume during the entire period is more than an order of magnitude larger than the source volume reduction defined by the GNSS data (Table 1). This difference can be explained assuming the establishment of a feedback loop, where the volume of material erupted through the eruptions induces a progressive pressure decrease in the reservoir at 2.6 km b. s. l. and, hence, exsolution and expansion of gas. In turn, the new gas partly replaces the erupted material, buffering the bulk volume reduction and leading to the overall mass decrease reflected in the gravity records.

Our results provide further evidence that, without support from gravimetry, the inversion of deformation data from active volcanoes may lead to incomplete or misleading inferences[13,16,38]. Therefore, whenever possible, gravity measurements of suitable quality should be performed to enhance the capabilities of the observation systems used to monitor and study active volcanoes.

Methods

Objective function for the inversion of the geophysical data. The joint inverse modeling of deformation and gravity data is based on the minimization of the following objective function:

$$O.F. = \frac{1}{|\Omega|} \sum_{i \in \Omega} \left(\frac{\hat{y}_i - y_i}{\sigma_{y_i}} \right)^2 \quad (7)$$

where, Ω is the set of measurements, $\hat{y}_i$ is the model prediction of the i-th measurement, y_i is the corresponding measured value and σ_{y_i} its associated uncertainty.

Table 4 Results from the application of the Akaike information criterion.

	K	WMSE	AIC
Mogi model	5	0.00468	4573.1
ECM	10	0.00403	5027.9

Number of involved parameters (K), Weighted Mean Squared Error (WMSE), and AIC value associated with the two considered models.

Checks on the data inversion procedure. We perform two analyses, aimed at checking the soundness of the adopted procedure for the joint inversion of gravity and deformation data.

Firstly, we explore the effect of changing the weights given to the residuals. These weights are randomly sampled from Gaussian distributions, each having (i) mean equal to the inverse of the uncertainty associated with the corresponding measurement and (ii) standard deviation equal to 10% of the mean. The sets of model parameters obtained considering the different weights are distributed within the 2-σ uncertainty intervals reported in Table 1.

Secondly, we check whether assuming an ellipsoidal source, rather than spherical, would lead to results significantly different from those we obtained (Table 1). We thus perform the joint inversion of the gravity and deformation data using a formulation that calculates the deformation field and the gravity changes due to the pressurization of a finite ellipsoidal cavity in a half-space (ECM[39]). The retrieved source parameters (Table 3), i.e., source position and changes in mass and volume, are very similar to those obtained with the Mogi[11] formulation. To establish which of the two formulations is more adequate to represent the process that generated the gravity and deformation data, we exploit the Akaike information criterion (AIC[40]). AIC estimates the relative amount of information lost by a given model and assigns higher quality (lower AIC value) to the models losing less information. The amount of lost information is evaluated on the grounds of a trade-off between goodness of the fit and simplicity of the model (i.e., number of independent variables used to build the model), implying that AIC deals with the risk of both overfitting and underfitting the observations. Application of AIC indicates that, in the present case, the Mogi formulation is to be preferred over the ECM[39]. Indeed, while the ellipsoidal cavity model provides a slightly better fit, in terms of WMSE, a lower AIC value is associated with the Mogi formulation, given the difference in the number of independent variables (Table 4).

Data availability

Data presented in this paper are available through this publicly accessible repository: https://zenodo.org/records/10124351.

Received: 11 March 2023; Accepted: 28 November 2023;
Published online: 12 December 2023

References

1. Calvari, S. & Nunnari, G. Comparison between automated and manual detection of lava fountains from fixed monitoring thermal cameras at Etna Volcano, Italy. *Remote Sens.* **14**, 239 (2022).
2. Carbone, D., Cannavò, F., Greco, F., Reineman, R. & Warburton, R. J. The benefits of using a network of superconducting gravimeters to monitor and study active volcanoes. *J. Volcanol. Geotherm. Res.* **124**, 4035–4050 (2019).
3. Antoni-Micollier et al. Detecting volcano-related underground mass changes with a quantum gravimeter. *Geophys. Res. Lett.* **49**, e2022GL097814 (2022).
4. Palano, M. et al. Etn@ref: A geodetic reference frame for Mt. Etna GPS networks. *Ann. Geophys* **53**, 49–57 (2010).
5. Herring, T. A., King, R. W. & McClusky, S. C. *Introduction to GAMIT/GLOBK, release 10.4.* (Massachusetts Institute of Technology, 2010).
6. Bruno, V. et al. Ground deformations and volcanic processes as imaged by CGPS data at Mt. Etna (Italy) between 2003 and 2008. *J. Geophys. Res.* **117**, B07208 (2012).
7. Chauhan, M. S., Cannavó, F., Carbone, D. & Greco, F. Insights into Mount Etna December 2018 eruption from joint inversion of deformation and gravity data. *Geophys. Res. Lett.* **47**, e2020GL087786 (2020).
8. Fores, B., Champollion, C., Le Moigne, N., Bayer, R. & Chéry, J. Assessing the precision of the iGrav superconducting gravimeter for hydrological models and karstic hydrological process identification. *Geophys. J. Int.* **208**, 269–280 (2017).
9. Audet, C. & Dennis, J. E. Analysis of generalized pattern searches. *SIAM J. Optim.* **13**, 889–903 (2003).
10. Cannavò, F. A new user-friendly tool for rapid modelling of ground deformation. *Comput. Geosci.* **128**, 60–69 (2019).
11. Mogi, K. Relations between the eruptions of various volcanoes and the deformations of the ground surfaces around them. *Bull. Earthquake Res. Inst.* **36**, 99–134 (1958).
12. Aloisi, M., Bonaccorso, A., Cannavò, F. & Currenti, G. M. Coupled short- and medium-term geophysical signals at Etna volcano: using deformation and strain to infer magmatic processes from 2009 to 2017. *Front. Earth Sci.* **6**, 109 (2018).
13. Greco, F., Bonforte, A. & Carbone, D. A long-term charge/discharge cycle at Mt. Etna volcano revealed through absolute gravity and GPS measurements. *J. Geod.* **96**, 101 (2022).
14. Williams, C. A. & Wadge, G. An accurate and efficient method for including the effects of topography in three-dimensional elastic models of ground deformation with applications to radar interferometry. *J. Geophys. Res. Solid Earth* **105**, 8103–8120 (2000).
15. Ferlito, C. et al. Dome-like behaviour at Mt. Etna: the case of the 28 December 2014 South East Crater paroxysm. *Sci. Rep.* **7**, 5361 (2017).
16. Carbone, D., Poland, M. P., Diament, M. & Greco, F. The added value of time-variable microgravimetry to the understanding of how volcanoes work. *Earth. Sci. Rev.* **169**, 146–179 (2017).
17. Bagnardi, M. et al. Gravity changes and deformation at Kīlauea Volcano, Hawaii, associated with summit eruptive activity, 2009–2012. *J. Geophys. Res.* **119**, 7288–7305 (2014).
18. Calvari, S., Cannavò, F., Bonaccorso, A., Spampinato, L. & Pellegrino, A. G. Paroxysmal explosions, lava fountains and Ash Plumes at Etna Volcano: eruptive processes and hazard implications. *Front. Earth Sci.* **6**, 107 (2018).
19. Sciotto, M. et al. Infrasonic gliding reflects a rising magma column at Mount Etna (Italy). *Sci. Rep.* **12**, 16954 (2022).
20. INGV-OE. Bollettino settimanale sul monitoraggio vulcanico, geochimico e sismico del vulcano Etna del 03/08/2021. https://www.ct.ingv.it/index.php/monitoraggio-e-sorveglianza/prodotti-del-monitoraggio/bollettini-settimanali-multidisciplinari
21. Longo, A., Garg, D., Papale, P. & Montagna, C. P. Dynamics of magma chamber replenishment under buoyancy and pressure forces. *J. Geophys. Res.* **128**, e2022JB025316 (2023).
22. Lisowski, M. Analytical volcano deformation source models. In *Volcano Deformation - New Geodetic Monitoring Techniques* (ed. Dzurisin, D.) 279-304 (Springer-Praxis Publishing, 2007).
23. Tiampo, K. F., Rundle, J. B., Fernandez, J. & Langbein, J. Spherical and ellipsoidal volcanic sources at Long Valley Caldera, California using a genetic algorithm inversion technique. *J. Volcanol.Geother. Res.* **102**, 189–206 (2000).
24. Hagiwara, Y. The Mogi model as a possible cause of the crustal uplift in the eastern part of Izu Peninsula and related gravity change. *Bull. Earthq. Res. Inst. Univ. Tokyo* **52**, 301–309 (1977).
25. González, P. J. & Palano, M. Mt. Etna 2001 eruption: new insights into the magmatic feeding system and the mechanical response of the western flank from a detailed geodetic dataset. *J. Volcanol.Geother. Res.* **274**, 108–121 (2014).
26. Papale, P., Moretti, R. & Barbato, D. The compositional dependence of the saturation surface of H_2O+CO_2 fluids in silicate melts. *Chem. Geol.* **229**, 78–95 (2006).
27. Spilliaert, N., Allard, P., Metrich, N. & Sobolev, A. V. Melt inclusion record of the conditions of ascent, degassing, and extrusion of volatile-rich alkali basalt during the powerful 2002 flank eruption of Mount Etna (Italy). *J. Geophys. Res. Solid Earth* **111**; https://doi.org/10.1029/2005JB003934 (2006).
28. Moretti, R. et al. Degassing vs. eruptive styles at Mt. Etna volcano (Sicily, Italy). Part I: Volatile stocking, gas fluxing, and the shift from low-energy to highly explosive basaltic eruptions. *Chem. Geol.* **482**, 1–17 (2018).
29. Métrich, N., Allard, P., Spilliaert, N., Andronico, D. & Burton, M. 2001 flank eruption of the alkali- and volatile-rich primitive basalt responsible for Mount Etna's evolution in the last three decades. *Earth Planet. Sci. Lett.* **228**, 1–17 (2004).
30. Lange, R. A. The effect of H_2O, CO_2, and F on the density and viscosity of silicate melts. *Rev. Mineral.* **30**, 331–370 (1994).
31. Kerrick, D. M. & Jacobs, G. K. A modified Redlich-Kwong equation for H_2O, CO_2, and H_2O-CO_2 mixtures at elevated pressures and temperatures. *Am. J. Sci.* **281**, 735–767 (1981).
32. Girona, T., Costa, F., Newhall, C. & Taisne, B. On depressurization of volcanic magma reservoirs by passive degassing. *J. Geophys. Res. Solid Earth* **119**, 8667–8687 (2014).
33. Pinel, V. & Jaupart, C. Some consequences of volcanic edifice destruction for eruption conditions. *J. Volcanol. Geotherm. Res.* **145**, 68–80 (2005).
34. Grosfils, E. B. Magma reservoir failure on the terrestrial planets: assessing the importance of gravitational loading in simple elastic models. *J. Volcanol. Geotherm. Res.* **166**, 47–75 (2007).
35. Geshi, N., Miyagi, I., Saito, G. & Conway, C. E. Caldera collapse thresholds correlate with magma chamber dimensions. *Sci Rep* **13**, 7463 (2023).
36. Miller, C. A., Le Mével, H., Currenti, G., Williams-Jones, G. & Tikoff, B. Microgravity changes at the laguna del maule volcanic field: Magma-induced stress changes facilitate mass addition. *J. Geophys. Res. Solid Earth* **122**, 3179–3196 (2017).
37. Carbone, D., Budetta, G., Greco, F. & Rymer, H. Combined discrete and continuous gravity observations at Mount Etna. *J. Volcanol. Geotherm. Res.* **123**, 123–135 (2003).
38. Battaglia, M., Gottsmann, J., Carbone, D. & Fernández, J. 4D volcano gravimetry. *Geophysics* **73**, WA3–WA18 (2008).
39. Nikkhoo, M. & Rivalta, E. Surface deformations and gravity changes caused by pressurized finite ellipsoidal cavities. *Geophys. J. Int.* **232**, 643–655 (2023).
40. Akaike, H. A new look at the statistical model identification. *IEEE Trans. Autom. Control* **19**, 716–723 (1974).
41. Middlemost, E. A. K. Iron oxidation ratios, norms and the classification of volcanic rocks. *Chem. Geol.* **77**, 19–26 (1989).
42. Efron, B. The jackknife, the bootstrap, and other resampling plans. *CBMS-NSF Regional Conference Series in Applied Mathematics* https://doi.org/10.1137/1.9781611970319 (1982).

Acknowledgements

This work was supported by the NEWTON-g project, which received funding from the EC's Horizon 2020 programme, under the FETOPEN-2016/2017 call (Grant Agreement No 801221). Support was also provided by the INGV-MIUR project 'Pianeta Dinamico (Dynamic Planet)—Working Earth'–Sub-project VT–DYNAMO—2023 and by the FIRST project ("Progetto Strategico Dipartimentale" of INGV). We are very grateful to M. Nikkhoo, E. Rivalta, and E. Grosfils for the helpful input they provided through constructive discussions. We are also indebted to technicians and technologists at INGV-OE, for enabling and improving the acquisition of GNSS and gravity data.

Author contributions

D.C. conceived the study and drafted the manuscript. F.C. performed the joint inversion of the deformation and gravity data. C.P.M. designed and conducted the geochemical modeling with SOLWCAD. F.G. contributed to the collection and analysis of the gravity data. D.C. wrote the paper, with contributions from all authors.

Competing interests

The authors declare no competing interests.

Additional information

Supplementary information The online version contains supplementary material available at https://doi.org/10.1038/s43247-023-01149-x.

Correspondence and requests for materials should be addressed to Daniele Carbone.

Peer review information *Communications Earth & Environment* thanks Matthew Head, Meredith Townsend, Kate Scholz, and the other, anonymous, reviewer(s) for their contribution to the peer review of this work. Primary Handling Editors: Emma Nicholson, Joe Aslin, and Aliénor Lavergne. A peer review file is available.